Low Speed Rotor/Fuselage Interactional Aerodynamics
NASA Research Cooperative Agreement NCC-1-367
Final Report

Richard W. Barnwell
Devon S. Prichard
Virginia Polytechnic Institute & State University
Virginia Consortium of Engineering & Science Universities
Hampton, VA 23666

July 18, 2003

1 Summary

This report presents work performed under a Cooperative Research Agreement between Virginia Tech and the NASA Langley Research Center. The work involved development of computational techniques for modeling helicopter rotor/airframe aerodynamic interaction. A brief overview of the problem is presented, the modeling techniques are described, and selected example calculations are briefly discussed.

2 Introduction

The aerodynamic interaction between the rotors and airframe of a helicopter presents an extremely complex modeling problem, and impacts the aerodynamic performance, structural loads and response, farfield noise, and handling qualities of the rotorcraft. The aerodynamic flowfield is inherently unsteady and three-dimensional, and the aerodynamic behavior of the airframe and rotors can be strongly coupled. Not only is the behavior of the viscous boundary layer on the airframe important, there are also tip vortices generated by the rotor blades which create highly localized flowfield gradients. The modeling dilemma has been to use simpler but practical prediction methods which fail to capture important flow characteristics, or use sophisticated brute-force computational modeling which requires rather extreme computing resources and approaches the limits of the existing numerical models.

Use of Euler/Navier-Stokes solvers for the interactional problem encounters several hurdles. Along with the motion of the rotor blades relative to the freestream, there is relative motion between the blades and the airframe, which ordinarily necessitates a moving grid capability. Having two grid patches with relative motion introduces a difficult interpolation and data transfer problem that can adversely affect the capture of the desired physical problem. There is a wide disparity in the largest and smallest length scales in the computational problem, particularly when tip vortices and boundary layers are to be modeled; this then creates the need for fine spatial resolution in the computational grids, thus also constraining the maximum computational time step that can be used. These spatial and temporal resolution constraints are countered by the existing practical computing power available, as well as stretch the capabilities of the numerical algorithms commonly available for solving the governing Euler/Navier-Stokes (ENS) equations. Given current computing technology, practical grid and time resolutions in an ENS solver will result in dissipation and diffusion of rotor tip vortices.

There are several publications in the literature which present prediction methods for the interactional problem. These methods can be divided into three categories; linear superposition, comprehensive CFD, and hybrid superposition/CFD methods. There have been many attacks on the interactional problem with superposition methods, [1. 2, 3, 4, 5, 6] for example. Since unsteady separation of the airframe boundary layer is a commonly encountered condition on helicopters, it is difficult at best to obtain aerodynamic loads on the airframe from superposition methods. Due to the extreme difficulty of the comprehensive CFD approach, there have been fewer publications using this category of methods [7, 8]. Recently there have been several publications using hybrid linear/CFD methods [9. 10, 11, 12, 13]. These hybrid methods have demonstrated a desirable tradeoff between fidelity of the problem physics and the computational resources required.

Vorticity confinement is a computational technique developed by John Steinhoff [14] for limiting the diffusion of vorticity in ENS flowfield computations. This technique has been applied by Steinhoff and his colleagues to a variety of complex flowfields with vorticity (for example. [15, 16, 17]).

The present work involves study of the vorticity confinement method, and modification and extension of the hybrid model of Boyd & Barnwell [10, 11, 12]. This model couples a sophisticated linear rotor wake aerodynamic model with a well-established unsteady 3-D ENS solver. The effect of the vorticity confinement term on various classic viscous flow problems with analytic or series solutions was also studied. Application of the hybrid model to arbitrary rotor/airframe configurations in arbitrary flight conditions necessitated comprehensive changes to the linear rotor wake model, the ENS solver, and the coupling mechanism between the two codes. The modifications to the prediction model and software are discussed, and results from certain example calculations are presented. Documentation concerning the actual use of the various computer programs is provided in a separate document entitled "GDWT/OVERFLOW Users' Guide".

3 Analytical Analyses of Vorticity Confinement

The following analyses apply vorticity confinement to incompressible, two-dimensional problems with flow in a predominant, or x, direction and gradients predominantly in the normal, or y. direction. For problems without pressure gradients the momentum equation in vector form is

$$\frac{\partial \vec{u}}{\partial t} + u\frac{\partial \vec{u}}{\partial x} + v\frac{\partial \vec{u}}{\partial y} = \nu\frac{\partial^2 \vec{u}}{\partial y^2} + \epsilon \hat{n}_{\nabla\omega} \times \vec{\omega}$$

where

$$\vec{u} = u\hat{\imath}$$

The coefficient ϵ in the last term, the nonphysical vorticity confinement term, has units of velocity. The vorticity vector is

$$\vec{\omega} = \left(\frac{\partial v}{\partial x} - \frac{\partial u}{\partial y}\right)\hat{k} \approx -\frac{\partial u}{\partial y}\hat{k}$$

The magnitude of this vector and the gradient of this magnitude are

$$\omega = |\vec{\omega}| = \left|\frac{\partial u}{\partial y}\right|$$

and

$$\nabla\omega = \frac{\partial}{\partial y}\left|\frac{\partial u}{\partial y}\right|\hat{\jmath} = s_{\nabla\omega}|\nabla\omega|\hat{\jmath}$$

where the coefficient $s_{\nabla\omega}$ has a value of +1 or -1. Thus the unit normal for the vector $\nabla\omega$ is

$$\hat{n}_{\nabla\omega} = \frac{\nabla\omega}{|\nabla\omega|} = s_{\nabla\omega}\hat{\jmath}$$

and the vorticity confinement term has the form $-s_{\nabla\omega}\epsilon\frac{\partial u}{\partial y}\hat{\imath}$. Consequently, the momentum equation in scalar form is

$$\frac{\partial u}{\partial t} + u\frac{\partial u}{\partial x} + \left(v + s_{\nabla\omega}\epsilon\right)\frac{\partial u}{\partial y} = \nu\frac{\partial^2 u}{\partial y^2}$$

Solutions with vorticity confinement are obtained for four classical problems in fluid mechanics: the Blasius problem, the shear flow problem, Couette flow, and the laterally oscillating plate problem. The last two solutions are analytic, and the first two are solved with the same numerical processes as the physical problems.

Comparisons of the first three solutions with their physical counterparts show that the confinement process concentrates more vorticity at boundaries than nature does, which is what the technique was designed to accomplish. As a result, the predictions with confinement for the boundary layer thickness for the Blasius problem and the shear layer thickness are smaller than the physical predictions, and the difference increases as the confinement coefficient and the local Reynolds number increase. For Couette flow, where vorticity is uniformly distributed in the physical problem, the effect of confinement is to distribute vorticity out of the interior and toward the walls. This effect also increases with increasing confinement coefficient and local Reynolds number.

It is characteristic of the laterally oscillating plate problem for the gradient of the magnitude of vorticity to change direction as a function of both time and distance from the plate. The effect of using vorticity confinement is to make the solution for fluid speed discontinuous with respect to distance from the wall where this direction reversal occurs.

3.1 The Blasius Problem

This problem involves the laminar motion of an incompressible fluid past a flat plate aligned with the undisturbed flow. The magnitude of the vorticity ω is largest at the surface of the plate and diminishes with distance from it. With the y coordinate chosen positive outward, ω will decrease with increasing y so that the coefficient $s_{\nabla\omega}$ has a value of -1, and the momentum equation is

$$u\frac{\partial u}{\partial x} + (v - \epsilon)\frac{\partial u}{\partial y} = \nu\frac{\partial^2 u}{\partial y^2}$$

This equation can be expressed in terms of a stream function with the substitution

$$u = U_\infty f'(x, \eta)$$

where

$$\eta \equiv y\sqrt{\frac{U_\infty}{2\nu x}}$$

where the prime represents differentiation with respect to the nondimensional coordinate η. The resulting equation is

$$f''' + \left(f + \epsilon\sqrt{\frac{2x}{U_\infty \nu}}\right) f'' = 2xf'\frac{\partial f'}{\partial x}$$

The solution for this stream function is not as simple as that for the conventional Blasius problem because the coefficient ϵ keeps it from depending only on the variable η. However, the equation can be simplified because the derivative $\frac{\partial f'}{\partial x}$ is negligible for this problem. The equation which results is

$$f''' + \left(f + \sqrt{2\bar{\epsilon}^2 Re_x}\right) f'' = 0$$

where the nondimensional coefficient $\bar{\epsilon}$ and local Reynolds number Re_x are

$$\bar{\epsilon} \equiv \frac{\epsilon}{U_\infty}$$

and

$$Re_x \equiv \frac{U_\infty x}{\nu}$$

The boundary conditions are the same as those for the conventional Blasius problem:

$$\lim_{y \to \infty} u(x,y) = U_\infty$$

and

$$u(x, y = 0) = v(x, y = 0) = 0$$

or

$$\lim_{\eta \to \infty} f'(x,\eta) = 1$$

and

$$f'(x, \eta = 0) = f(x, \eta = 0) = 0$$

Because the conventional Blasius solution for the velocity profile $u/U_\infty = f'(\eta)$ is independent of the local Reynolds number, the profiles are the same at each station along the plate, and the boundary layer is said to be in equilibrium. However, the profiles obtained with vorticity confinement depend on the local Reynolds number through the parameter $\bar{\epsilon}^2 Re_x$ and become increasingly steeper than the Blasius profiles as the Reynolds number increases. This effect reduces the boundary layer thickness and is consistent with the concept of "confining" vorticity.

With $\bar{\epsilon} = 0.001$ and $Re_x = 100,000$ as representative values, the value of 0.1 results for the parameter $\bar{\epsilon}^2 Re_x$. Velocity profiles for the values $\bar{\epsilon}^2 Re_x = 0.1$ and $\bar{\epsilon}^2 Re_x = 1.0$ are compared with the Blasius profile in Figure 1.

3.2 The Shear Flow Problem

Two parallel, incompressible laminar flows of different speed are brought into contact and allowed to interact without any pressure gradient. Assume that the upper undisturbed flow speed U_+ is larger than the lower speed U_-. The magnitude of the vorticity ω is largest in both flows at the interface where $y \equiv 0$, and it diminishes in both regions with distance from the interface so that $s_{\nabla\omega} = -1$ in the upper region and $s_{\nabla\omega} = +1$ in the lower region. Thus, the momentum equations for the upper and lower flows are written as

$$u\frac{\partial u}{\partial x} + (v - \epsilon)\frac{\partial u}{\partial y} = \nu\frac{\partial^2 u}{\partial y^2}$$

and

$$u\frac{\partial u}{\partial x} + (v + \epsilon)\frac{\partial u}{\partial y} = \nu\frac{\partial^2 u}{\partial y^2}$$

respectively, and the corresponding stream function equations are

$$f''' + \left(f + \sqrt{2\bar{\epsilon}^2 Re_x}\right) f'' = 0$$

and

$$f''' + \left(f - \sqrt{2\bar{\epsilon}^2 Re_x}\right) f'' = 0$$

where the stream function f is defined as

$$u = U_+ f'(x, \eta)$$

and the nondimensional coordinate η is defined as

$$\eta \equiv y\sqrt{\frac{U_+}{2\nu x}}$$

Also, the nondimensional vorticity confinement coefficient and Reynolds number are defined as

$$\bar{\epsilon} \equiv \frac{\epsilon}{U_+}$$

and

$$Re_x \equiv \frac{U_+ x}{\nu}$$

The boundary conditions are

$$\lim_{y \to +\infty} u(x, y) = U_+$$

$$\lim_{y \to -\infty} u(x, y) = U_-$$

and

$$v(x, y = 0) = 0$$

or

$$\lim_{\eta \to +\infty} f'(x, \eta) = 1$$

$$\lim_{\eta \to -\infty} f'(x, \eta) = \frac{U_-}{U_+}$$

and

$$f(x, \eta = 0) = 0$$

As with the physical solution, the stream function f for the confinement solution and its first two derivatives f' and f'' are continuous at the interface. However, the third derivative f''' is discontinuous at the interface with the multiple values

$$f'''(x, \eta = \pm 0) = \mp\sqrt{2\bar{\epsilon}^2 Re_x} f''(x, \eta = 0)$$

The confinement solution for the velocity profile $u/U_+ = f'$ with $\bar{\epsilon}^2 Re_x = 0.1$ and $\bar{\epsilon}^2 Re_x = 1.0$ are compared with the physical solution in Figure 2. Also, results for the normal velocity function $\sqrt{2Re_x}v/U_+$ with and without confinement are compared in Figure 3.

3.3 The Couette Flow Problem

Two parallel plates, which are separated by a distance h and have a viscous fluid between them, move parallel to each other with relative speed U_w. The magnitude of the vorticity ω for the physical problem is U_w/h, so the divergence of ω is zero everywhere. When vorticity confinement is used, the vorticity is more concentrated or "confined" at the walls where it is generated, and the divergence of ω vanishes only at the midpoint.

Let the x axis be located midway between the plates so that the y coordinates of the upper and lower plates are $+h/2$ and $-h/2$, respectively. Also let the origin be moving relative to the two plates so that the velocities of the upper and lower plates are $+U_w/2$ and $-U_w/2$, respectively. The momentum equation and boundary conditions for the physical problem are

$$\frac{d^2u}{dy^2} = 0$$

and

$$u(y = \pm h/2) = \pm\frac{U_w}{2}$$

and the physical solution is

$$u(y) = U_w\frac{y}{h}$$

When confinement is used, the magnitude of the vorticity ω is largest at the walls so that it increases as the upper wall is approached from below and as the lower wall is approached from above. Consequently, $\partial\omega/\partial y > 0$ and $s_{\nabla\omega} = +1$ for $+h/2 \geq y \geq 0$, and $\partial\omega/\partial y < 0$ and $s_{\nabla\omega} = -1$ for $0 \geq y \geq -h/2$.

The momentum equation with confinement is

$$\nu\frac{d^2u}{dy^2} - \epsilon\frac{du}{dy} = 0$$

for $+h/2 \geq y \geq 0$ and

$$\nu\frac{d^2u}{dy^2} + \epsilon\frac{du}{dy} = 0$$

for $0 \geq y \geq -h/2$. The boundary conditions are the same as those for the physical problem. The solution is

$$u(y) = \frac{U_w}{2}\frac{\exp\left(\frac{y}{h}\bar{\epsilon}Re_h\right) - 1}{\exp\left(\frac{1}{2}\bar{\epsilon}Re_h\right) - 1}$$

for $+h/2 \geq y \geq 0$ and

$$u(y) = -\frac{U_w}{2}\frac{\exp\left(-\frac{y}{h}\bar{\epsilon}Re_h\right) - 1}{\exp\left(\frac{1}{2}\bar{\epsilon}Re_h\right) - 1}$$

for $0 \geq y \geq -h/2$, where the nondimensional confinement parameter and Reynolds number are

$$\bar{\epsilon} \equiv \frac{\epsilon}{U_w}$$

and

$$Re_h \equiv \frac{U_w h}{\nu}$$

With values of $\bar{\epsilon} = 0.001$ and $Re_h = 1000$ as representative, the parameter $\bar{\epsilon}Re_h$ has the value 1.0. Results for solutions with the confinement parameter values $\bar{\epsilon}Re_h = 1.0$, $\bar{\epsilon}Re_h = 5.0$, and $\bar{\epsilon}Re_h = 10.0$ are compared with the physical solution in Figure 4.

3.4 The Oscillating Plate Problem

An infinite flat plate oscillates laterally with the sinusoidal speed $U\cos\sigma t$, causing the viscous fluid above it to oscillate also, but with a time lag based on y, the vertical distance from the plate. Because the plate is infinite and the motion is lateral, there is no dependence on the horizontal, or x, coordinate, and there is no motion in the vertical, or y, direction. Therefore, the momentum equation is

$$\frac{\partial u}{\partial t} = \nu\frac{\partial^2 u}{\partial y^2} + s_{\nabla\omega}\epsilon\frac{\partial u}{\partial y}$$

or

$$\frac{\partial u}{\partial \tau} = \frac{1}{2}\frac{\partial^2 u}{\partial \eta^2} + s_{\nabla\omega}\bar{\epsilon}\frac{\partial u}{\partial \eta}$$

where the nondimensional parameters τ, η, and $\bar{\epsilon}$ are

$$\tau \equiv \sigma t$$

$$\eta \equiv \sqrt{\frac{\sigma}{2\nu}}y$$

$$\bar{\epsilon} \equiv \frac{\epsilon}{\sqrt{2\nu\sigma}}$$

The momentum equation including confinement can be reduced to the physical equation with the transformation

$$u = v\exp\left(-s_{\nabla\omega}\bar{\epsilon}\eta\right)$$

The equation for v is

$$\frac{\partial v}{\partial t} = \frac{1}{2}\frac{\partial^2 v}{\partial \eta^2} - \frac{\bar{\epsilon}^2}{2} v$$

The last term, which varies as the square of the small parameter $\bar{\epsilon}$, can be ignored so that the equation for v reduces to the physical equation for u. The most general solution for v is

$$v(\eta, \tau) = \exp(-\eta) \left\{ A \cos(\tau - \eta) + B \sin(\tau - \eta) \right\}$$

The solution for u which satisfies the boundary condition is

$$u(\eta, \tau) = \exp\left[-(1 + s_{\nabla_\omega})\bar{\epsilon}\right] \cos(\tau - \eta)$$

The value of the parameter s_{∇_ω} depends on the y derivatives of the speed u and the magnitude of vorticity ω. These derivatives are

$$\frac{\partial u}{\partial y} = \sqrt{\frac{\sigma}{2\nu}} U \exp\left[-(1 + s_{\nabla_\omega}\bar{\epsilon})\eta\right] \left\{ \sin(\tau - \eta) - (1 + s_{\nabla_\omega}\epsilon) \cos(\tau - \eta) \right\}$$

and

$$\frac{\partial \omega}{\partial y} = \pm \frac{\sigma}{\nu} U \exp\left[-(1 + s_{\nabla_\omega}\bar{\epsilon})\eta\right] \left\{ -\sin(\tau - \eta) + s_{\nabla_\omega}\epsilon \left[\cos(\tau - \eta) - sin(\tau - \eta)\right] \right\}$$

where the + sign applies if $\frac{\partial u}{\partial y} > 0$. If the overall sign of $\frac{\partial \omega}{\partial y}$ is positive, the value of s_{∇_ω} is 1, otherwise it is -1.

The difficulty with the confinement solution for u for this problem is that it is not continuous in the variable η across boundaries where s_{∇_ω} changes sign. The equations for $\frac{\partial u}{\partial y}$ and $\frac{\partial \omega}{\partial y}$ show that the sign of $\frac{\partial \omega}{\partial y}$ is determined by trigonometric functions of the variable $(\tau - \eta)$. At boundaries where s_{∇_ω} changes, the magnitude of u changes by the exponential factor $\exp(2\bar{\epsilon}\eta)$.

4 Original Interactional Aerodynamic Model

A new method for predicting rotor/airframe aerodynamic interaction was developed in the original Cooperative Agreement [10, 11, 12]. This method coupled a linear aerodynamic model for the rotor with an unsteady, 3-D compressible RANS (Reynolds-Averaged Navier-Stokes) solver. This type of coupled analysis is generically called a hybrid method. When applied to the difficult rotor/fuselage interaction problem, this sort of hybrid method is intended to offer a computationally feasible compromise between the simplicity of linear superposition methods and the currently impractical comprehensive CFD approach. The method available at the start of the task extension has already been documented at length, so only a brief overview will be provided in this report.

The linear aerodynamic model used in the previous and present work is the Finite-State Wake Model (FSWM) originated by Peters, as described in the paper by Peters and He [18]. The Finite-State Wake Model is also called the Generalized Dynamic Wake Theory (GDWT) model, which is the nomenclature used in the present work. The essence of the GDWT model is a pressure potential solution to a linearized form of the Euler equations. The pressure potential solution recast the time-varying and 3-D problem into a form using a family of orthogonal shape functions for the radial coordinate and harmonic series analysis for the azimuthal coordinate. In its current form, the field solution relates the flowfield, including the rotor-induced downwash, to a prescribed pressure discontinuity across the rotor disk. Lifting line theory is used to obtain closure by providing an estimate for the pressure discontinuity due to a prescribed downwash at the rotor disk. A simple trim algorithm was added to enable the GDWT code to compute the required control pitch inputs needed to match a desired thrust, pitch moment, and roll moment on the rotor. The result of a GDWT analysis are the aerodynamic loads on the rotor blades (in lifting line form) and the downwash at the rotor disk for the isolated rotor. The original GDWT code was "hard-wired" for 4-bladed rotors of clockwise rotation.

The Navier Stokes solver used in the previous work was OVERFLOW version 1.8l. This code solves the unsteady, 3-D, compressible RANS equations on structured, overset grids. The code was modified to add two new boundary conditions which can be applied on a circular grid plane embedded in a cylindrical grid block. By applying a pressure discontinuity across that grid plane, a jump in the specific energy is added which simulates the effect of a thrusting rotor in the flowfield. By combining a rotor grid block with a fuselage grid, the effect of the rotor on the fuselage can be approximated, as well as the effect of the fuselage on the rotor. The boundary condition intended for performing crude steady-state predictions replaces the set of individual rotor blades with a continuous circular "actuator disk." The boundary condition intended to model the unsteady blade passage effect approximates the rotating rotor blades with moving wedges of pressure discontinuity that rotate at the proper rate. Upon completion of an OVERFLOW analysis, the downwash at the rotor disk is obtained.

By computing the difference between the OVERFLOW-predicted downwash and the GDWT-predicted downwash, a correction is obtained which can be used in a following

GDWT calculation. This provides a first-order approximation to the rotor/fuselage interactional effect. Continuing the process of coupled GDWT and OVERFLOW computations yields a hybrid method which runs efficiently and robustly. The method was found to compare very well with high-quality wind tunnel data of unsteady fuselage pressures taken on the ROBIN model [10, 11, 12].

5 Modifications to the Interactional Model

There have been a variety of modifications to the interactional aerodynamics model. The modifications encompass the GDWT code, the modified OVERFLOW code, and the coupling mechanism between the two. These modifications have been made to generalize the method to rotors of arbitrary blade number and to improve the robustness of the rotor trim analysis in the GDWT program.

5.1 Modifications to GDWT/OVERFLOW Coupling

The most pervasive modifications to the GDWT/OVERFLOW system were a result of the requirement to handle the main rotor of the Comanche scale model. That rotor has 5 blades, but the original prediction system was limited to modeling rotors for which the blade count was a power of two (*i.e.* 1, 2, 4, ...). The GDWT program requires that the number of azimuth stations on the rotor disk be a power of 2, regardless of the number of blades on the rotor. However, the way the present method models rotors in the Navier-Stokes analysis requires that the number of azimuth stations in the rotor block of the CFD grid be an integer multiple of the blade count. Since those two constraints on azimuthal resolution can rarely be satisfied by a single azimuth angle distribution, a method for decoupling the azimuthal resolution of the two codes was developed and implemented.

The original GDWT code converted blade sectional airloads into a constant-chordwise pressure distribution, which was read in by the modified OVERFLOW code and used directly on the actuator disk boundary condition. The GDWT program was modified to write out blade sectional airloads in tabular form, and the modified OVERFLOW was changed to read in the new airloads file and interpolate the airloads data azimuthally from the GDWT discretization scheme to the OVERFLOW grid.

The computation of the OVERFLOW-predicted downwash at the rotor disk was modified to allow the user to input the number of vertical grid planes across which the rotor-induced downwash is averaged and written out to disk files for subsequent use by the GDWT code. The GDWT code was modified to allow the user to input the number of OVERFLOW time steps per revolution and the number of revolutions of downwash data to read in and use in the GDWT analysis.

The GDWT program was also modified to write out a text file containing the rotor trim state at the end of each trim analysis, and likewise modified to read in the trim datafile at the beginning of each restart run. These modifications usually reduce the necessary number of trim iterations performed by the GDWT code when doing iterative coupling.

A Unix shell script was developed to automate the iterative coupling between the GDWT and OVERFLOW codes for simple problem configurations.

5.2 Modifications to the GDWT Method

There have been a variety of modifications to the GDWT program. The maximum number of azimuthal harmonics and radial shape functions has been increased. The code has been extended to handle rotor blades with nonlinear twist distributions as well as linear distributions. The code has been modified to reconcile the "handedness" of the rotor rotation (*i.e.* whether the rotor's direction of rotation is clockwise or counterclockwise as viewed from above) with the sign of the roll moment. The program now generates several new output datafiles for plotting blade airloads and wake-induced downwash. The code was also modified to allow for arbitrary rotor orientation relative to the freestream (and thus can now handle axial as well as edgewise flight). The GDWT code itself was modified to use 64-bit precision for all floating-point variables. The lifting-line model has been generalized to handle rotors with arbitrary angles-of-attack, including conditions of axial flow.

There have been a series of modifications to the trim mechanism in the GDWT program. The minimization objective function, which sums the difference between the computed and target values of thrust coefficient, roll moment coefficient, and pitch moment coefficient, was modified to increase the relative scale of the roll and pitch moment contributions. This was driven by the relative magnitude of the coefficients of thrust versus the two moments, which is a consequence of the nondimensionalization used in defining the coefficients. The forces used to compute the thrust and moments was changed from computations based on the τ_c arrays [18] to computations based on the lifting line model. This change ensured consistency between the forces used in the rotor trim analysis within the GDWT code and the forces used to model the rotor in the modified OVERFLOW code. In the course of running certain cases it was found necessary to limit the computed increment in the collective and cyclic pitch inputs. Hard-wired limits of 2 degrees for collective pitch angle changes and 1 degree for the lateral and longitudinal pitch angle changes were added to the code. These limiters help prevent unstable trim iteration sequences. Lastly, modifications were made to the mechanism for incrementing the three control angles (collective, lateral cyclic, and longitudinal cyclic pitch angle) in the algorithm for computing the controls sensitivity matrix. As the trim iteration progresses, the control angle increments are reduced from the starting increment of 2 degrees down to 0.25 degrees after 30 trim iterations. This code modification accelerates the trim solution convergence process for many cases. By changing the compilation options, the older trim algorithm can be restored to compare recent calculations with the previous method. For several cases tested, the trim state and downwash using the new code with the older trim algorithm activated were identical to those computed with the original code.

5.3 Modifications to the OVERFLOW Method

The modified OVERFLOW program has had several changes and enhancements to its method for modeling rotors in the flowfield. In conjunction with modifications to the GDWT code, OVERFLOW has been modified to handle both righthanded and lefthanded rotors. In order to handle rotors of arbitrary blade count, coding has been added to read in the tabular rotor airloads file generated by GDWT and interpolate the data azimuthally to match the azimuthal resolution of the rotor grid block. Note that, due to the mechanism by which the GDWT/OVERFLOW system models moving rotor blades within the Navier-Stokes solution, unsteady flowfield calculation in OVERFLOW is constrained to have the azimuthal resolution in the rotor grid block align with the time resolution. In other words, while the current software can handle an arbitrary blade count and rotor rotational speed, the Navier-Stokes calculations must be configured to have appropriate temporal and azimuthal resolution (so that one time step equals the time interval for a blade to travel from one azimuthal grid line to the next). Also, the OVERFLOW method has been modified to have a limited ability to model multiple rotors on the flowfield. If all rotors have equal rotational speeds (as in tandem and tiltrotor designs), then all rotors can be modeled with either the steady or unsteady rotor loading method. If not, then one rotor must be designated for the unsteady analysis and the rest modeled with the steady actuator disk method.

5.4 Other Software

A number of utility programs have been developed in the course of testing the aforementioned modeling and code modifications. Examples include programs for reading GDWT and OVERFLOW output files and organizing airloads and downwash data for plotting, a grid generation program designed to generate rotor and background grids for OVERFLOW, a tool to visualize the CFL number on the computational grids, and programs to convert grid and solution files between various data formats.

6 Example Calculations

Several example cases have been created and used to verify that modifications to the interactional method properly handle the desired interactional problems. Preliminary calculations have also been made for the Comanche model helicopter. These cases correspond to various input and output files delivered to NASA along with the source code and Users' Guide.

6.1 Effect of GDWT Force & Moment Trim Algorithm

To demonstrate the effect of the changes to the trim algorithm in the GDWT code, basic calculations were made to demonstrate the change in computed trim and downwash. A hypothetical case was constructed of a typical 4-bladed helicopter rotor of rectangular planform, 10 degrees linear twist rate, an aspect ratio of 10, a tip Mach number of 0.5, an advance ratio of 0.1, an angle-of-attack of 0 degrees, and a thrust coefficient of 0.0102.

Table 1 shows the differences in the trimmed control pitch inputs and area-weighted downwash between the old trim algorithm and the new algorithm; as can be seen, there are substantial differences in the rotor trim state and resulting rotor-induced downwash. Attempts to determine the cause of the discrepancy were unsuccessful, though preliminary calculations indicated a sensitivity to the spatial and temporal resolution. Since the modifications to the coupling mechanism required a sectional lift-based coupling rather than a chordwise distributed pressure coupling as originally coded, it was felt that consistency between the rotor model in OVERFLOW and GDWT was critical and thus the current software is configured to use the new algorithm.

6.2 GDWT Grid Resolution Study

A brief study of radial and azimuthal resolution was performed to ensure that subsequent calculations were reasonably accurate. Basic calculations were performed using different values of the `Nharm`, `Nrad`, and `Nazm` input parameters. Note that the number of radial shape functions is constrained to a value of `Nharm` + 1, thus there is a connection between `Nharm` and `Nrad`. For a given value of `Nharm` there is a minimum value of `Nrad` needed to ensure that the radial shape functions have sufficient points to define their series coefficients. Likewise, `Nharm` and `Nazm` are related such that there is a minimum `Nazm` required for a given `Nharm`.

A hypothetical case was constructed of a typical 4-bladed helicopter rotor of rectangular planform, 10 degrees linear twist rate, an aspect ratio of 10, a tip Mach number of 0.5, an advance ratio of 0.1, an angle-of-attack of 0 degrees, and a thrust coefficient of 0.0102.

Figure 5 shows the sensitivity of blade sectional airloads at 70% radius to `Nrad` values of 30, 60, and 90, given `Nharm`=8 and `Nazm`=256. The radial stations were constantly spaced along the blade. Very little sensitivity in the overall airloads to radial resolution is seen. Figure 6 shows a similar sensitivity comparison for `Nazm` values of 64, 128, and 256. Somewhat more sensitivity is seen, but the general character of the airloads remains the same. Figure 7 shows the sensitivity to `Nharm` values of 4, 8, 12, and 16, with `Nrad`=60 and `Nazm`=256. A substantial amount of sensitivity is seen in the Nharm parameter, along with the beginnings of solution instability for `Nharm`=16. Unfortunately, the memory footprint and CPU time requirements increase rapidly for large values of `Nharm`, so no effort was made to find a stable solution for higher values of `Nharm`.

6.3 Propeller in Axial Flight

A case with an isolated propeller in purely axial flight was developed to validate certain aspects of the coding changes performed in the present work. A hypothetical case was constructed of a 4-bladed propeller of rectangular planform, 60 degrees linear twist rate, an aspect ratio of 10, a tip Mach number of 0.75, an advance ratio of 0.1, an angle-of-attack of -90 degrees (*i.e.* typical propeller working conditions), and a thrust coefficient of 0.015. Performing a single GDWT analysis for this axially symmetric condition allowed identification of numerical precision issues that were addressed by the conversion to strictly 64-bit precision.

Table 2 presents the downwash across the rotor disk computed by OVERFLOW, given an initial GDWT disk loading. The `Joffset` parameter is a user input which determines the grid planes above and below the pressure jump plane on which the total downwash is averaged and output for subsequent use in a GDWT analysis. A `Joffset` of 3 seems to provide the best downwash average for the grids that have been used in the present work.

Figure 8 shows a convergence history for the coupling between GDWT and OVERFLOW over 6 coupling iterations (the "0-th" iteration is an initialization run of GDWT and then steady and unsteady OVERFLOW calculations, and iterations 1 through 5 are subsequent coupled calculations with GDWT and unsteady OVERFLOW runs). The collective pitch angle θ_0 and the area-weighted average downwash at the rotor disk, both computed by GDWT, converge very quickly. Since there are no bodies or other rotors in this problem, the downwash correction used by GDWT only derives from modeling differences between GDWT and OVERFLOW. Some of the differences include modeling of wake contraction in OVERFLOW versus no contraction in GDWT, blade chordwise discretization error in OVERFLOW versus an accurate blade chord used in GDWT, and tip vortex resolution limits in OVERFLOW due to normal and radial grid spacing versus radial resolution of the tip loading in GDWT due to decomposing the total blade loading into the radial shape functions.

6.4 Tiltrotor in Ground Effect

A simple case of a tiltrotor aircraft similar to the V-22 Osprey in ground effect was developed to demonstrate the ability of the GDWT/OVERFLOW system to predict both multirotor flowfields and aircraft/ground aerodynamic interaction. Two Osprey-like counter-rotating proprotors, of 5.8 meter radius with the starboard proprotor having righthanded rotation and the portside proprotor lefthanded rotation, were modeled in the flowfield without any fuselage/wing/tail but with the presence of a ground plane. Flight speed was about 54 knots, and the rotor hubs were located 6.9 meters above the ground plane. The aerodynamic loads on the rotors were modeled by GDWT with each rotor in isolated flight, then the total flowfield was modeled with the unsteady compressible Euler equation solver in OVERFLOW using two cylindrical rotor blocks embedded in a simple background grid.

Figure 9 shows contours of pressure coefficient on the grid planes immediately below the actuator disk plane after 5 rotor revolutions in the unsteady analysis. The ground plane is drawn with constant color simply to provide a geometric reference. This plot verifies that the indexing logic handles 3-bladed rotors correctly, and that the OVERFLOW solver is properly capturing the lateral symmetry of the problem. Figure 10 shows pressure coefficient contours on the ground plane, with the rotor disks drawn as a shaded surface to visualize their location relative to the ground pressure. Figure 11 shows contours of vorticity magnitude on a constant-Y plane in the background grid, which cuts through the advancing side of the portside rotor. The proprotor actuator disk planes and the ground plane are drawn as shaded surfaces to provide geometric reference. While concentrated vorticity representing convecting tip vortices can be seen, the vortices dissipate rapidly due to numerical dissipation.

6.5 Comanche Model Main Rotor in Isolated Flight

An isolated rotor computation for the Comanche model main rotor was performed to demonstrate handling of counter-clockwise rotation and arbitrary blade count in the modified GDWT/OVERFLOW system. The flight conditions chosen were those of run 60, point 459 of the 2002 test in the Langley 14x22 wind tunnel. GDWT was executed once, and OVERFLOW was run once with steady rotor modeling and once with unsteady rotor modeling, using the steady calculation as an initial condition. The OVERFLOW calculations were performed with a coarse two-block grid, one grid being the cylindrical grid block containing the rotor disk, and one grid being a Cartesian background block with uniform spacing in all three directions. Figure 12 shows pressure coefficient contours on a grid plane just below the rotor disk, after 480 time steps, with the bottom plane of the background grid drawn as a shaded surface to provide geometric reference. The contours show the chordwise distribution of loading, the presence of 5 blades, and the proper counter-clockwise rotation.

6.6 Comanche Model Main and Tail Rotor Interaction

A crude model for the Comanche model tail "rotor" was created and a preliminary calculation made for the main and tail rotors using OVERFLOW for run 60 as described above. Although the actual model has a ducted fan in a complex housing, the current calculation was simplified to use a simple actuator disk with no empennage or housing. The main rotor was modeled with the unsteady rotor model (IBTYP=444) and the tail rotor modeled with a constant pressure discontinuity over the disk (IBTYP=442). Given a main rotor thrust coefficient of 0.0084, an estimate of 0.00070 for the tail rotor torque coefficient was generated using Figure 4-5 of Gessow & Myers [20]. Given the tail rotor torque coefficient and lever arm between the main and tail rotors, required tail rotor thrust was computed and thus the needed constant pressure differential required to generate that thrust. Figure 13 shows the pressure coefficients on grid planes below the main and tail rotors as well as the ground plane.

6.7 Comanche Model Fuselage in Isolated Flight

A multiblock grid for the Comanche model fuselage (*sans* vertical and horizonal stabilizers) was received from Mark Sanetrik of Lockheed Martin. The normal spacing was generated to be suitable for Euler calculations. Due to the rather complex fuselage surface definition, this grid contains 61 grid blocks. To evaluate this grid, an outer background block was generated to enclose the fuselage grid and the OVERFLOW code was run for 500 steady iterations and 480 unsteady time steps for the flow conditions of run 60.

Figure 14 shows the fuselage surface geometry definition, with the boundaries between the body-fitted grid blocks denoted with lines. This figure illustrates the complexity of the fuselage grid. Figure 15 shows contours of pressure coefficient on the fuselage surface, and Figure 16 shows a closeup of pressure coefficient contours on the nose of the fuselage. There are a number of unexpected pressure gradients present in the contour data. While some occur in regions where the grid topology is complex, for example the angular transition between the tail boom and the fenestron housing, others occur in areas where the body geometry is relatively monotonic and grid topology is smooth, such as on the tail boom aft of the engine bulges. The cause of these gradients in the predicted surface pressure is not known; one potential cause is a poor interpolation stencil generated by the PEGASUS program.

6.8 Comanche Model Main Rotor/Fuselage Interaction

A preliminary main-rotor/fuselage interaction case for the Comanche model was computed using the interactional model for run 60. 500 steady iterations were computed, followed by 480 unsteady time steps equivalent to two rotor revolutions. Figure 17 shows pressure coefficient contours on the fuselage surface and a grid plane immediately beneath the main rotor. Again the bottom plane of the outer background grid was drawn as a shaded surface to provide geometric reference. As with the isolated fuselage calculation, there are anomalous gradients in the fuselage surface pressure distribution. The flowfield near the main rotor shows some aerodynamic interaction with the pylon on top of the fuselage.

7 Summary

Analytical studies of the vorticity confinement model have been performed, and have shown that the the confinement model in low-speed viscous flow calculations does affect the flowfield solution, including important flow characteristics such as boundary layer thickness and viscous wall shear.

The GDWT/OVERFLOW interactional aerodynamic model has been extended to model a wider range of problems. Capabilities now include rotors of arbitrary blade count, rotors of counterclockwise as well as clockwise rotation, blades with nonlinear twist distributions, flowfields with multiple rotors, and rotors and propellers in flight at arbitrary angles-of-attack. The trim algorithm in the GDWT code has been substantially modified.

Several utility programs have been developed for use in conjunction with the interactional aerodynamic prediction system. Unix shell scripts for compiling source code and running executable programs have been developed. Example cases to demonstrate capabilities and validate the models have been created. An extensive users' guide has been written to document the coupling process, describe all of the pertinent inputs, and provide guidance in program usage. Initial calculations have been made to verify the various programs can correctly model the interactional aerodynamic flowfield around the Comanche scale model.

References

[1] Mavris, D. N., Liou, S. G., Komerath, N. M., and McMahon, H. M., "Measurement and Computation of the Velocity Field of a cylinder in the Wake of a Rotor in Forward Flight," presented at the 20th AIAA Fluid Dynamics, Plasma Dynamics, and Lasers Conference, June, 1989.

[2] Egolf, T. A., and Lorber, P. F., "An Unsteady Rotor/Fuselage Interactional Method," presented at the Americn Helicopter Society Specialists' Meeting on Aerodynamics and Aeroacoustics, February, 1987.

[3] Berry, J. D., "A Method of Computing the Aerodynamic Interactions of a Rotor-Fuselage Configuration in Forward Flight," PhD dissertation, Georgia Institute of Technology, May 1990.

[4] Quackenbush, T. R., Lam, C-M. G., Bliss, D. B., and Katz, A., "Computational methods for the Analysis of Rotor Wake/Airframe Interactions," Continuum Dynamics Inc. Report No. 91-02, 1991.

[5] Crouse, G. L. Jr., "An Analytical Study of Unsteady Rotor/Fuselage Interaction in Hover and Forward Flight," PhD dissertation, University of Maryland, November, 1992.

[6] Boyd, D. D. Jr., Brooks, T. F., Burley, C. L., and Jolly, J. R. Jr., "Aeroacoustic Codes for Rotor Harmonic and BVI Noise - CAMRAD.Mod1/HIRES: methodology and Users' manual," NASA TM 207640, 1998.

[7] Meakin, R., "Moving Body Overset Grid Methods for Complete Aircraft Tiltrotor Simulations," presented at the 11th AIAA Computational Fluid Dynamics Conference, June, 1993.

[8] Potsdam, M. A. and Strawn, R. C., "CFD Simulations of Tiltrotor Configurations in Hover," Proceedings of the 58th Annual Forum of the American Helicopter Society, Montreal, Canada, June 11-13, 2002.

[9] Chaffin, M. S.; and Berry, J. D., "Navier-Stokes Simulation of a Rotor Using a Distributed Pressure Disk Method," Presented at the American Helicopter Society 51st Annual Forum, May 9-11, 1995.

[10] Boyd, Jr., D.D., and Barnwell, R.W., "Rotor-Fuselage Interactional Aerodynamics: An Unsteady Rotor Model," Proceedings of the 54th Annual American Helicopter Society Forum, May 1998.

[11] Boyd, Jr., D.D., "Rotor-Fuselage Interaction Aerodynamics: A New Computation Model," PhD thesis, Virginia Polytechnic Institute and State University, July 1999.

[12] Boyd, Jr., D. Douglas, Barnwell, Richard W., and Gorton, Susan A., "A Computational Model for Rotor-Fuselage Interactional Aerodynamics," 38th AIAA Aerospace Sciences Meeting and Exhibit, Reno, Nevada, January 2000.

[13] Moulton, M. A., Bridgeman, J. O. and Caradonna, F. X., "Development of an Overset/Hybrid CFD Method for the Prediction of Hovering Performance," Proceedings of the 53rd Annual Forum of the American Helicopter Society, April-May 1997.

[14] Steinhoff, J., Vorticity Confinement: A New Technique for Computing Vortex Dominated Flows, Frontiers of Computational Fluid Dynamics, D. Caughey and M. Hafez, editors, John Wiley and Sons, 1994.

[15] Steinhoff, John, Wenren, Yonghu, Mersch, Thomas, and Senge, Heinrich, "Computational Vorticity Capturing: Application to Helicopter Rotor Flow," AIAA Paper number 92-0056, 1992.

[16] Wenren, Yonghu, Steinhoff, John, Wang, Lesong, Fan, Meng, and Xiao, Min, "Application of Vorticity Confinement to the Prediction of Flow over Complex Bodies," AIAA Paper number 2000-2621, 2000.

[17] Bridgeman, John Osburn, and Dietz, William E., "Vorticity Confinement Modeling of Dynamic Stall with Tight Structural Coupling," presented at the American Helicopter Society Aerodynamics, Acoustics, and Test Evaluation Specialists Meeting, San Francisco, CA, Jan 23-25, 2002.

[18] Peters, David A., and He, Cheng Jian, "Finite State Induced Flow Models Part II: Three-Dimensional Rotor Disk," Journal of Aircraft, Volume 32, Number 2, March-April, 1995.

[19] P.G. Buning, W.M. Chan, K.J. Renze, D.L. Sondak, I.-T. Chiu, and J.P. Slotnick, "OVERFLOW User's Manual, Version 1.6ab," NASA Ames Research Center, Moffett Field, CA, January 1993.

[20] Gessow, Alfred, and Myers, Garry C., Aerodynamics of the Helicopter, Frederick Ungar Publishing Co., 1981.

Trim Algorithm	θ_0, deg	θ_{1c}, deg	θ_{1s}, deg	**Downwash, re** ΩR
old algorithm	8.972576	2.297601	-1.930369	0.04766
new algorithm	7.712145	2.409383	-1.453357	0.04177

Table 1: Effect of trim algorithm on computed trim and downwash

`Joffset`	**Downwash, re** ΩR
1	0.0447118
2	0.0447135
3	0.0488628
4	0.0479212
5	0.0477425

Table 2: Effect of `Joffset` parameter on steady-state OVERFLOW downwash

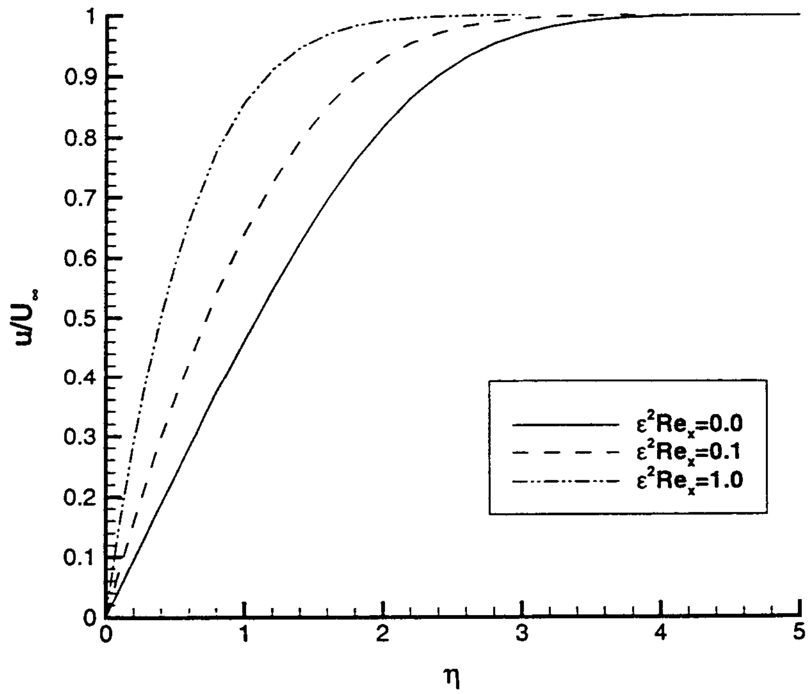

Figure 1: Velocity profiles of the physical and confined solutions for the Blasius problem

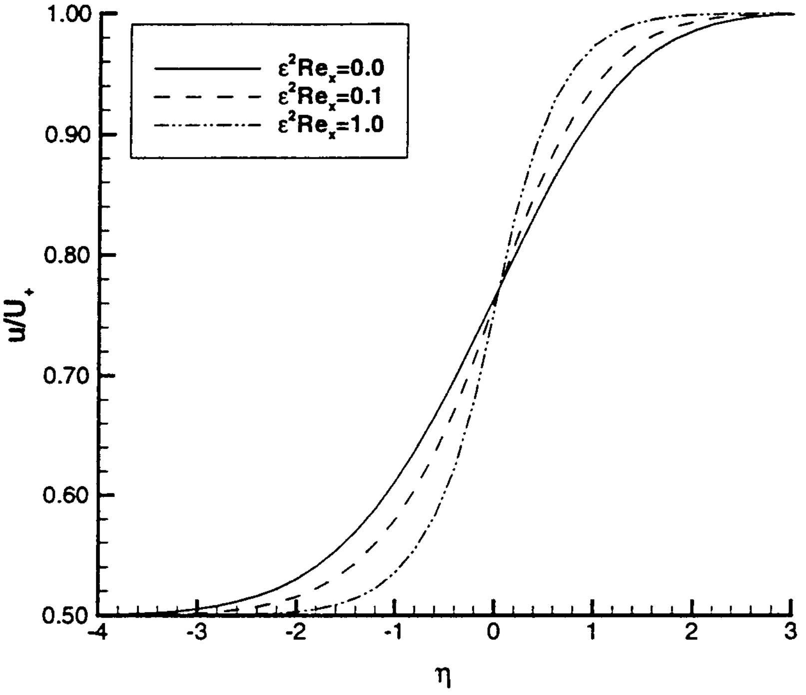

Figure 2: Tangential velocity profiles of the physical and confined solutions for the shear flow problem

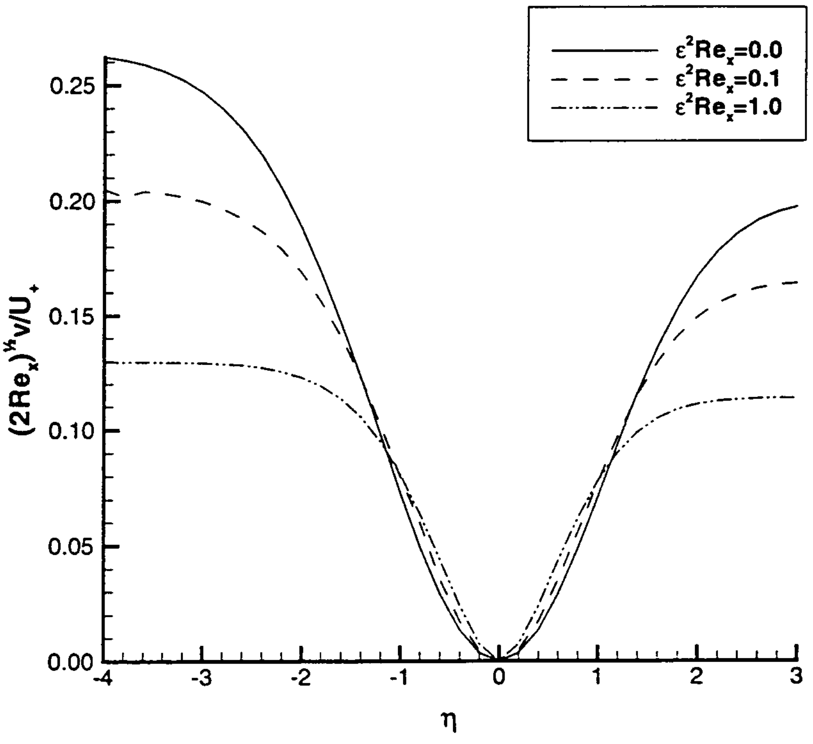

Figure 3: Normal velocity profiles of the physical and confined solutions for the shear flow problem

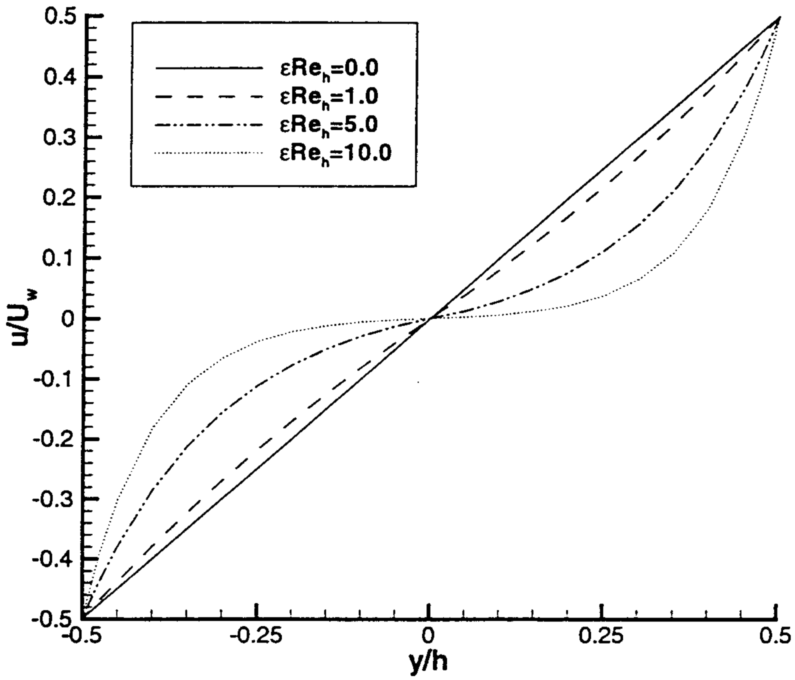

Figure 4: Tangential velocity profiles of the physical and confined solutions for the Couette flow problem

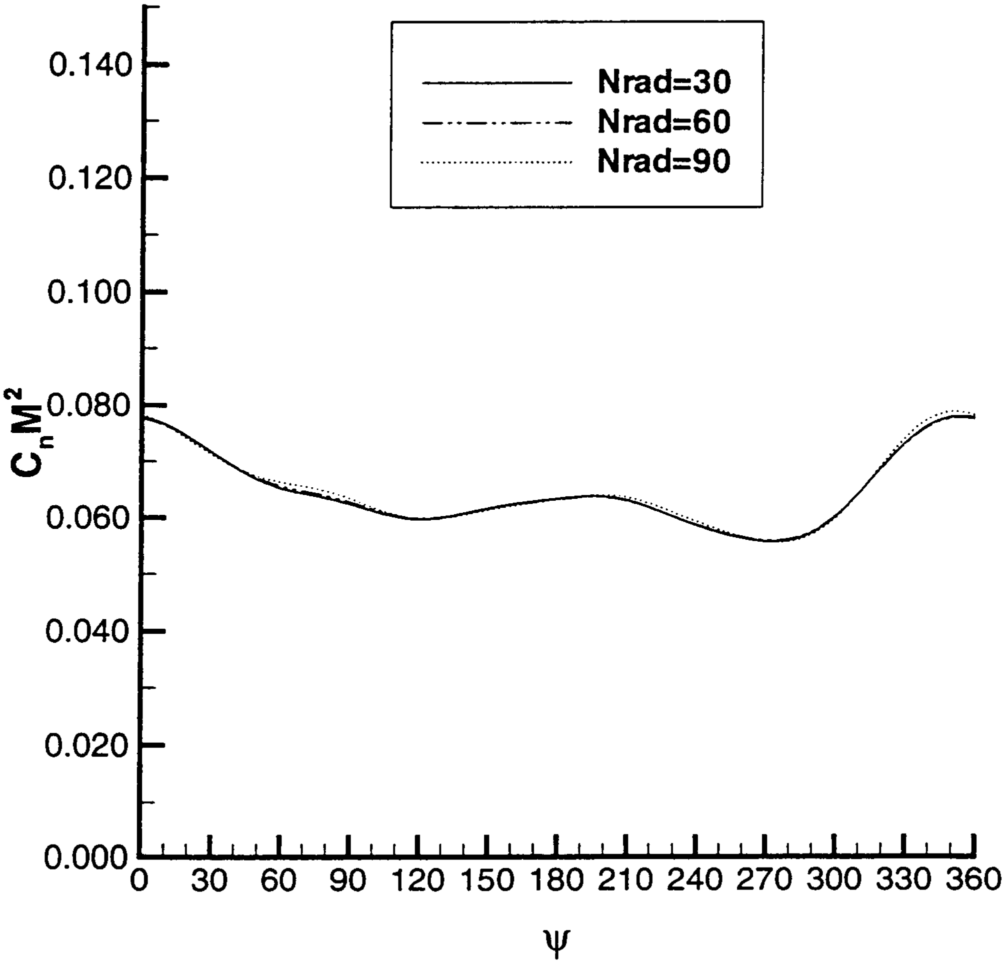

Figure 5: Sensitivity of blade sectional airloads at r/R=0.70 due to variations in `Nrad` for `Nharm=8` and `Nazm=256`

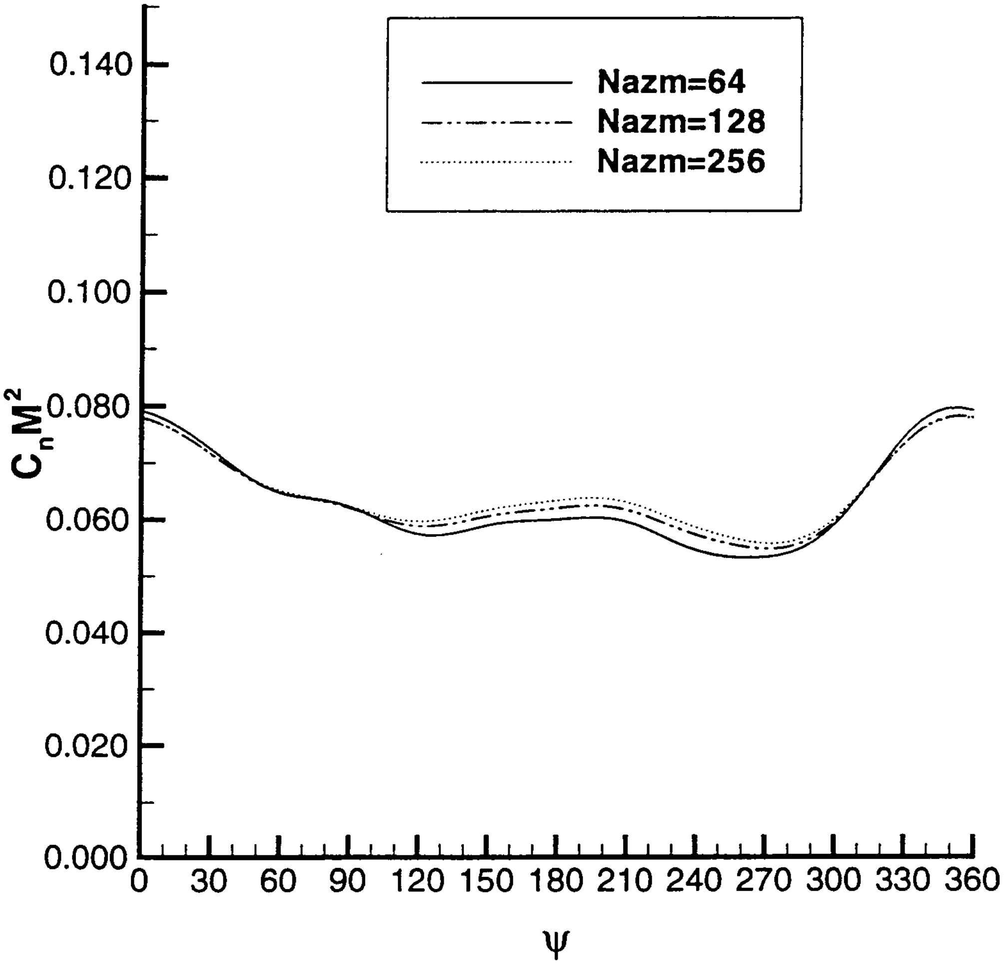

Figure 6: Sensitivity of blade sectional airloads at r/R=0.70 due to variations in `Nazm` for `Nharm=8` and `Nrad=60`

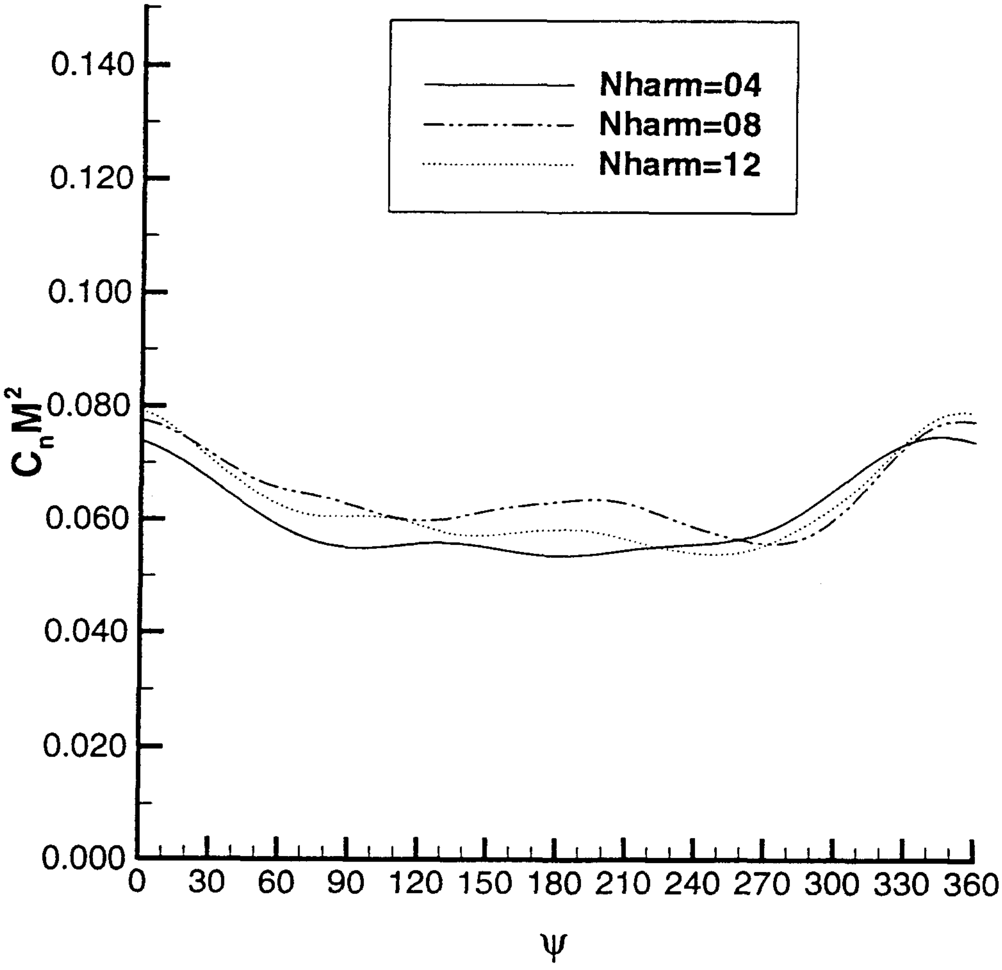

Figure 7: Sensitivity of blade sectional airloads at r/R=0.70 due to variations in `Nharm` for `Nrad=60` and `Nazm=256`

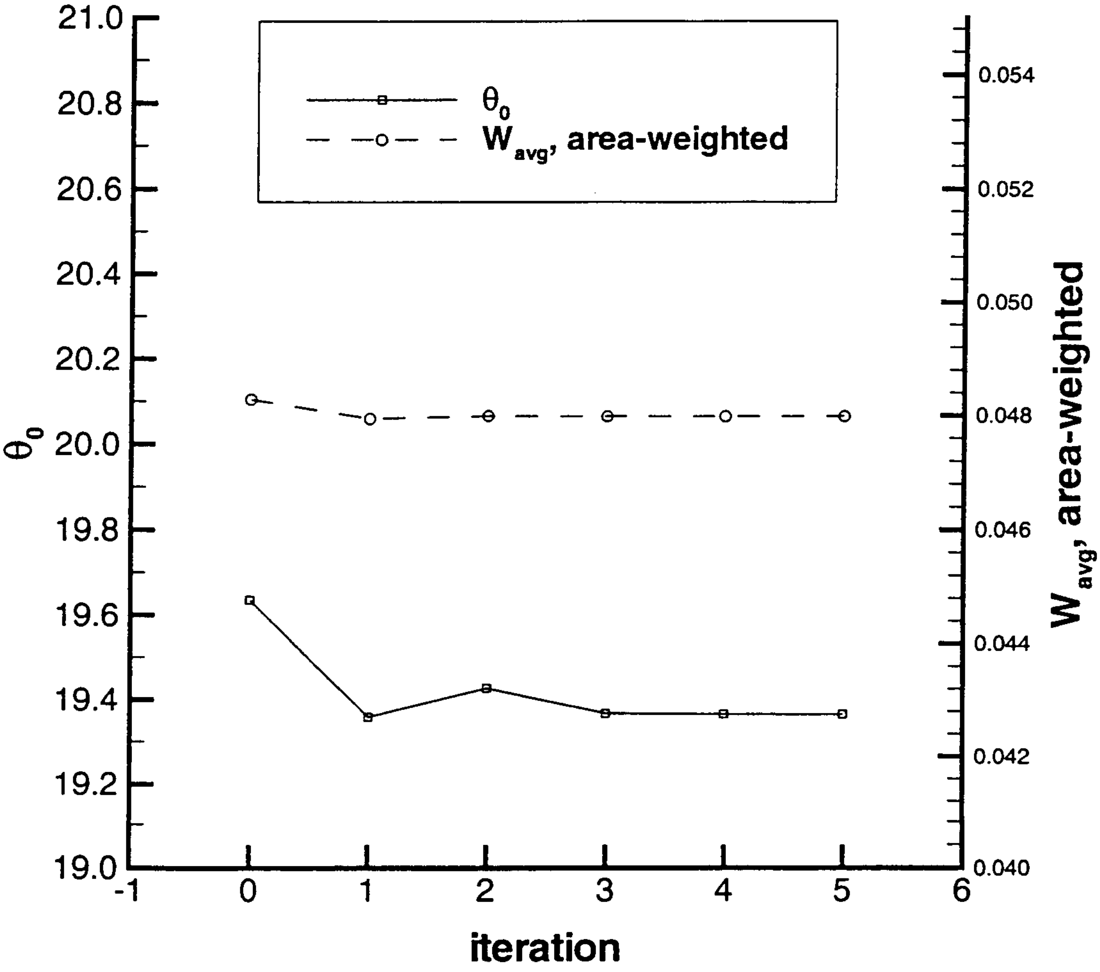

Figure 8: GDWT/OVERFLOW coupling convergence history for axial flight propeller case

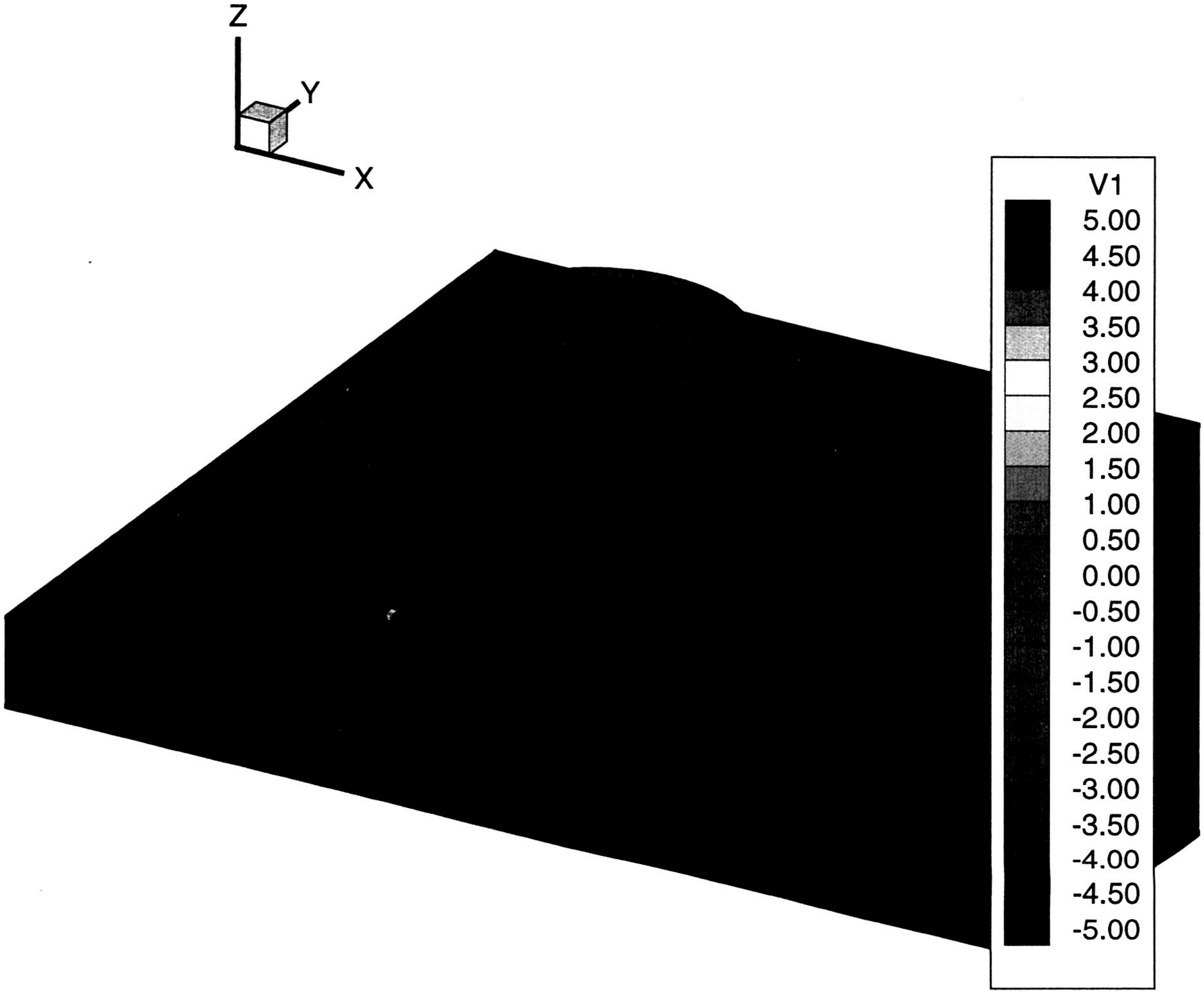

Figure 9: Unsteady calculations of pressure coefficient on grid planes below the rotors for the tiltrotor example case

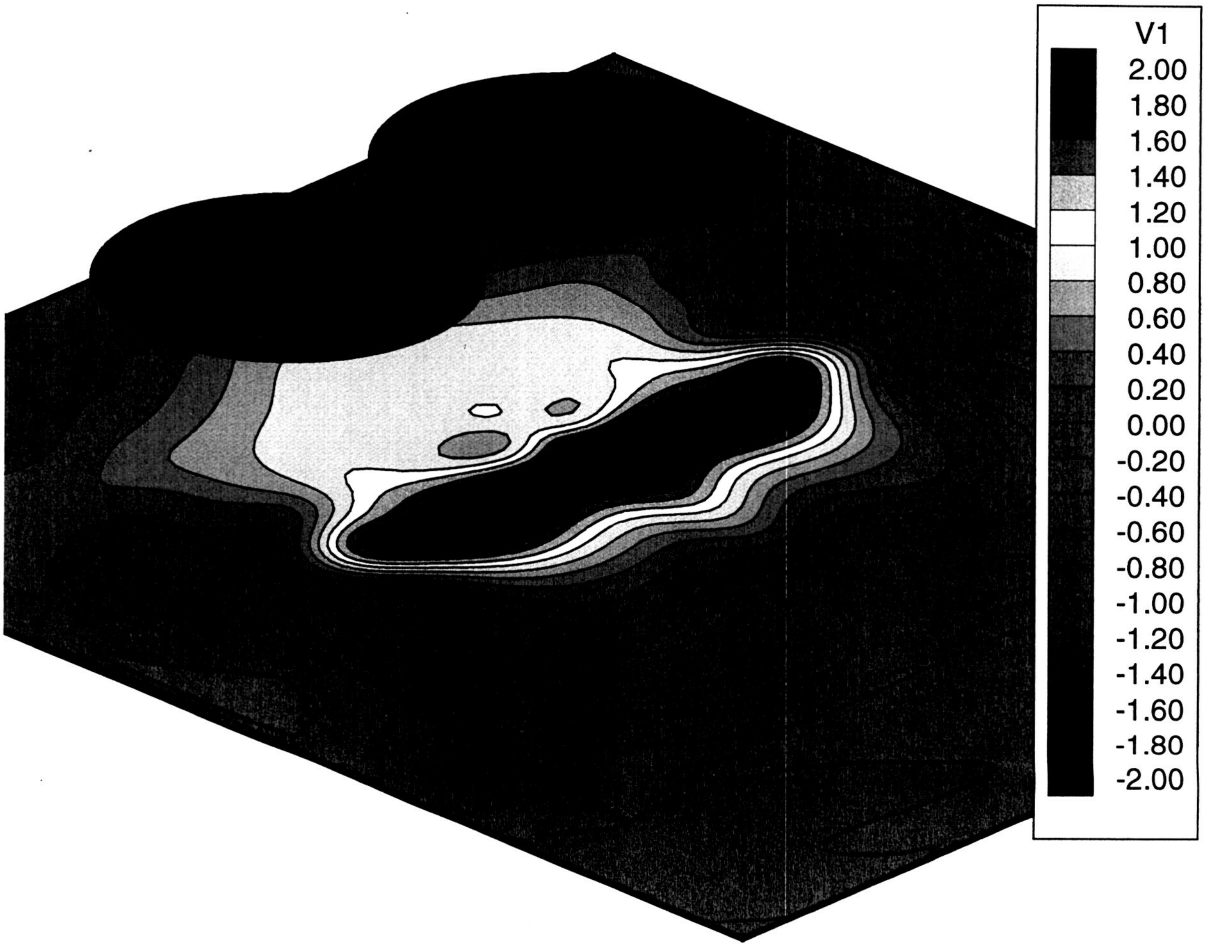

Figure 10: Unsteady calculations of pressure coefficient on the ground plane for the tiltrotor example case

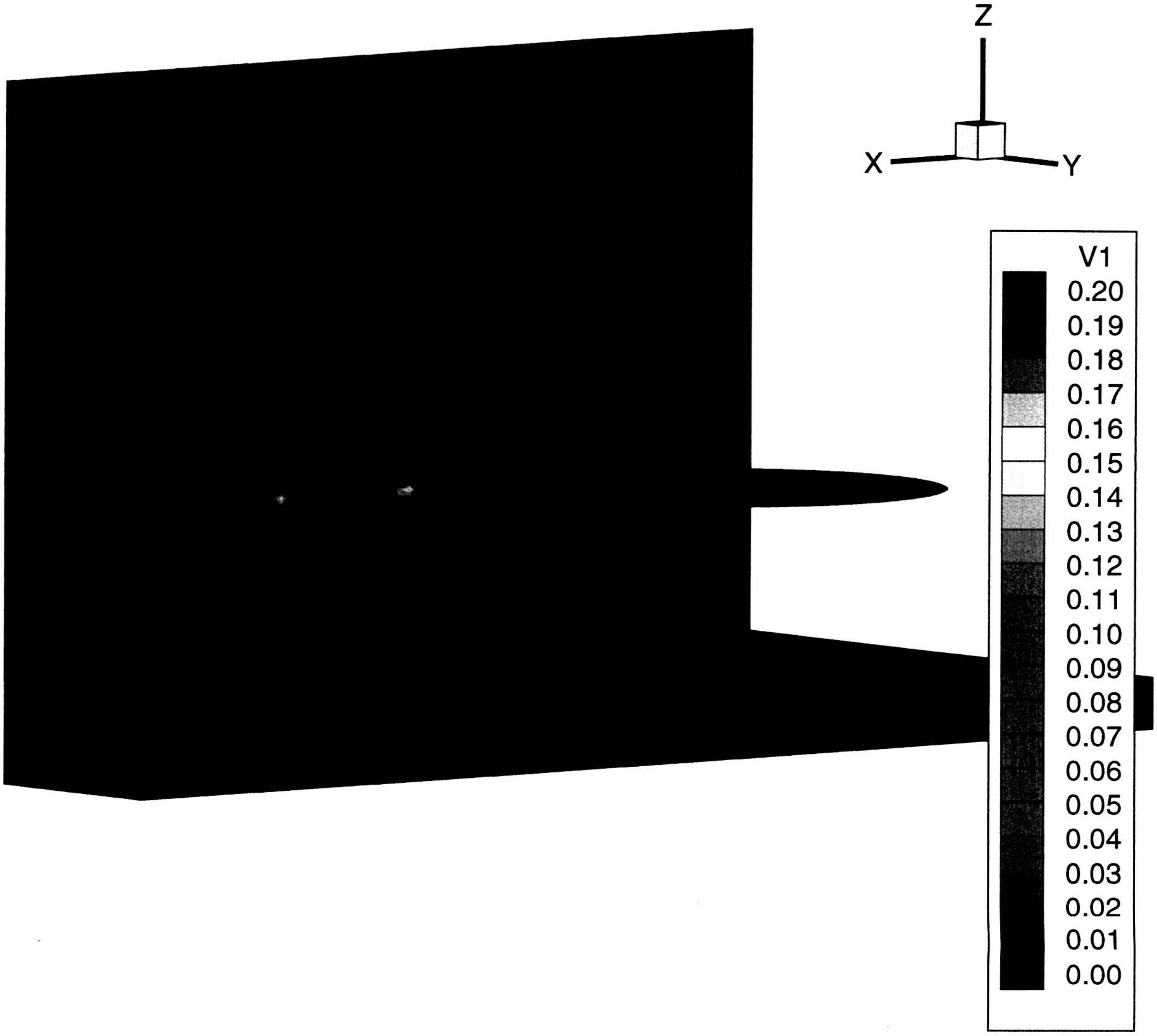

Figure 11: Unsteady calculations of vorticity magnitude on a constant-Y plane for the tiltrotor example case

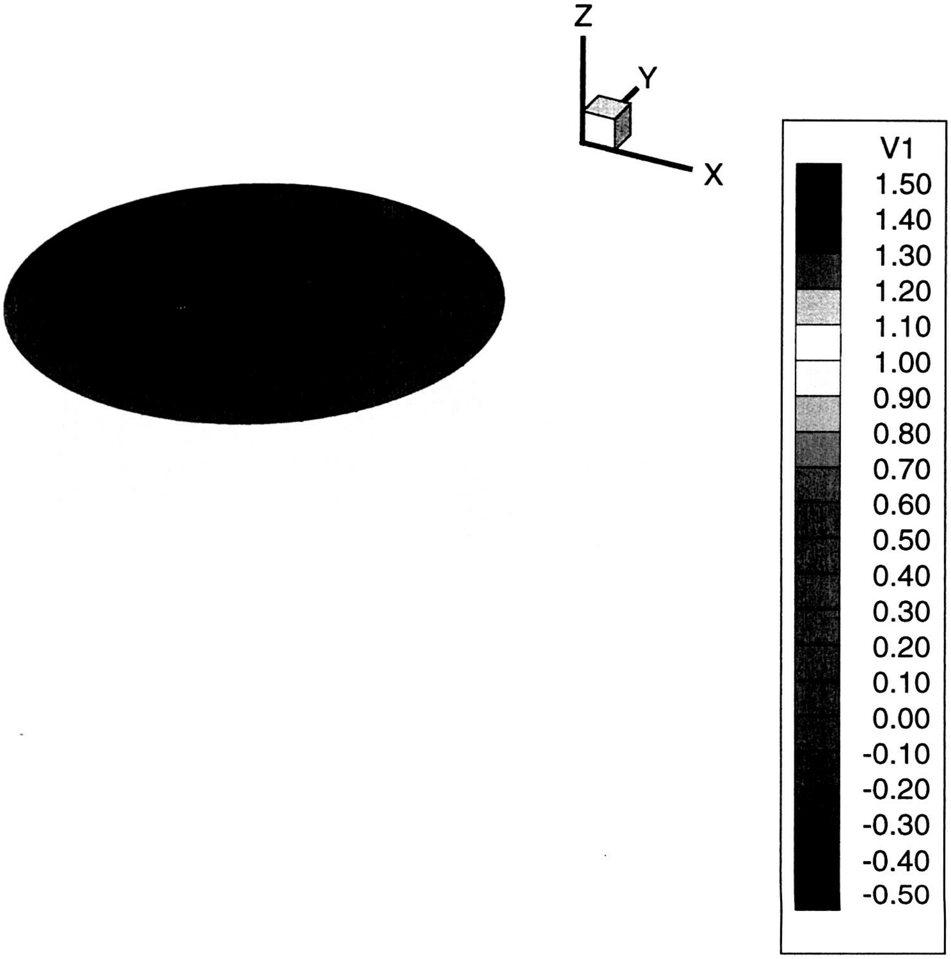

Figure 12: Unsteady calculations of pressure coefficient on a grid plane below the rotor for the Comanche model main rotor in forward flight

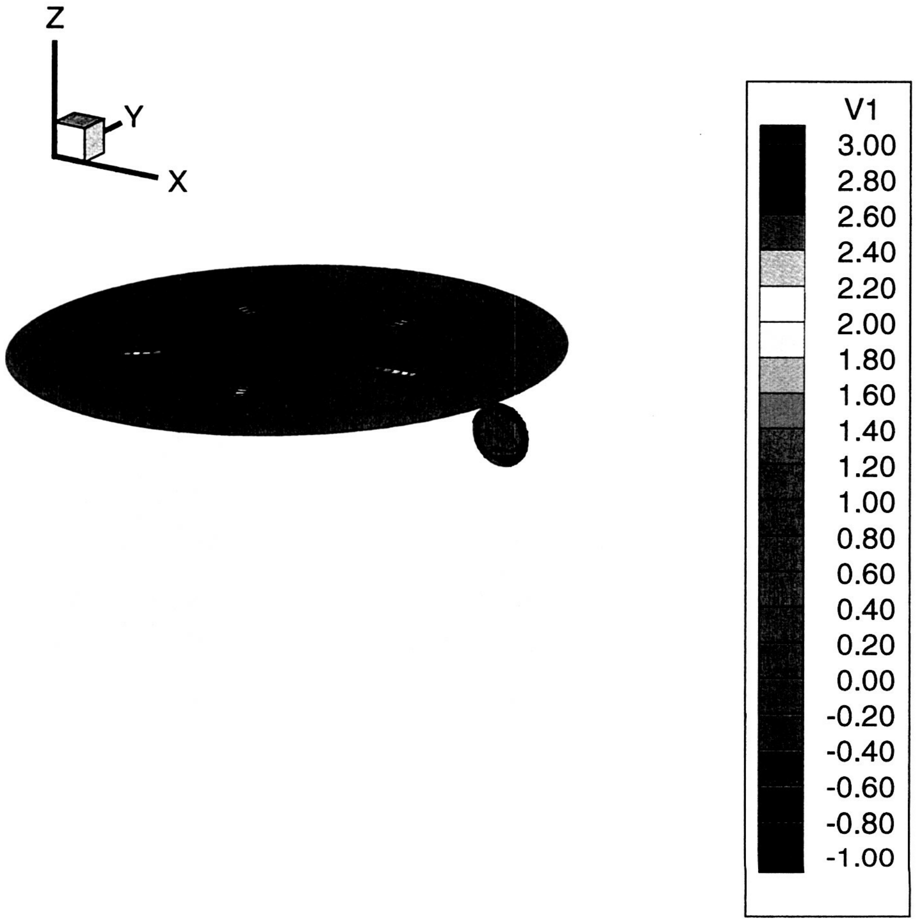

Figure 13: Unsteady calculations of pressure coefficient on grid planes below the main and tail rotors for the Comanche model in forward flight

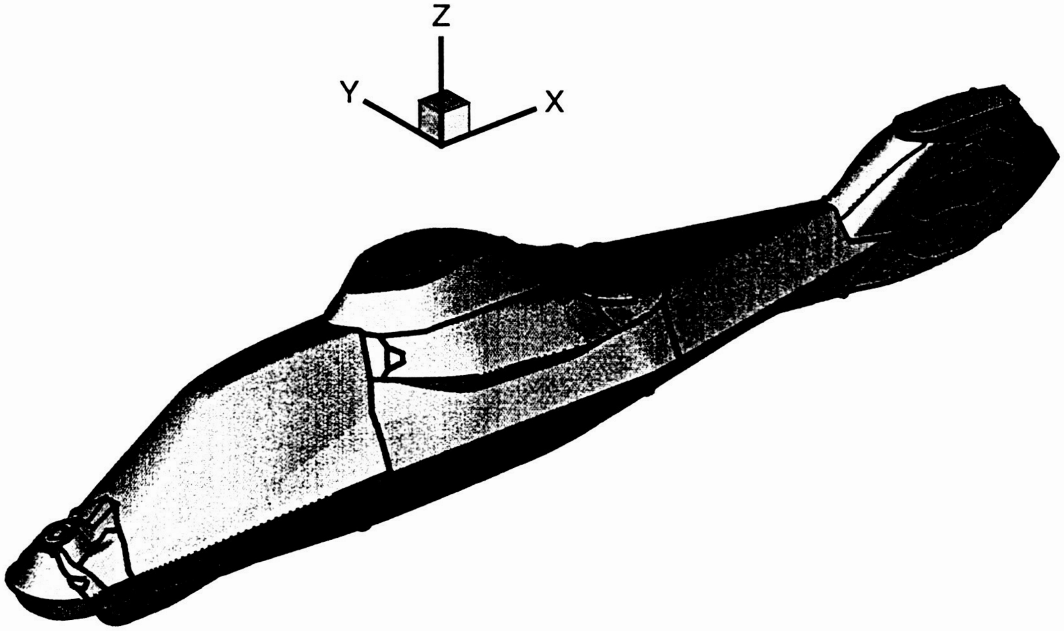

Figure 14: Comanche model fuselage surface definition with grid block boundary edges shown

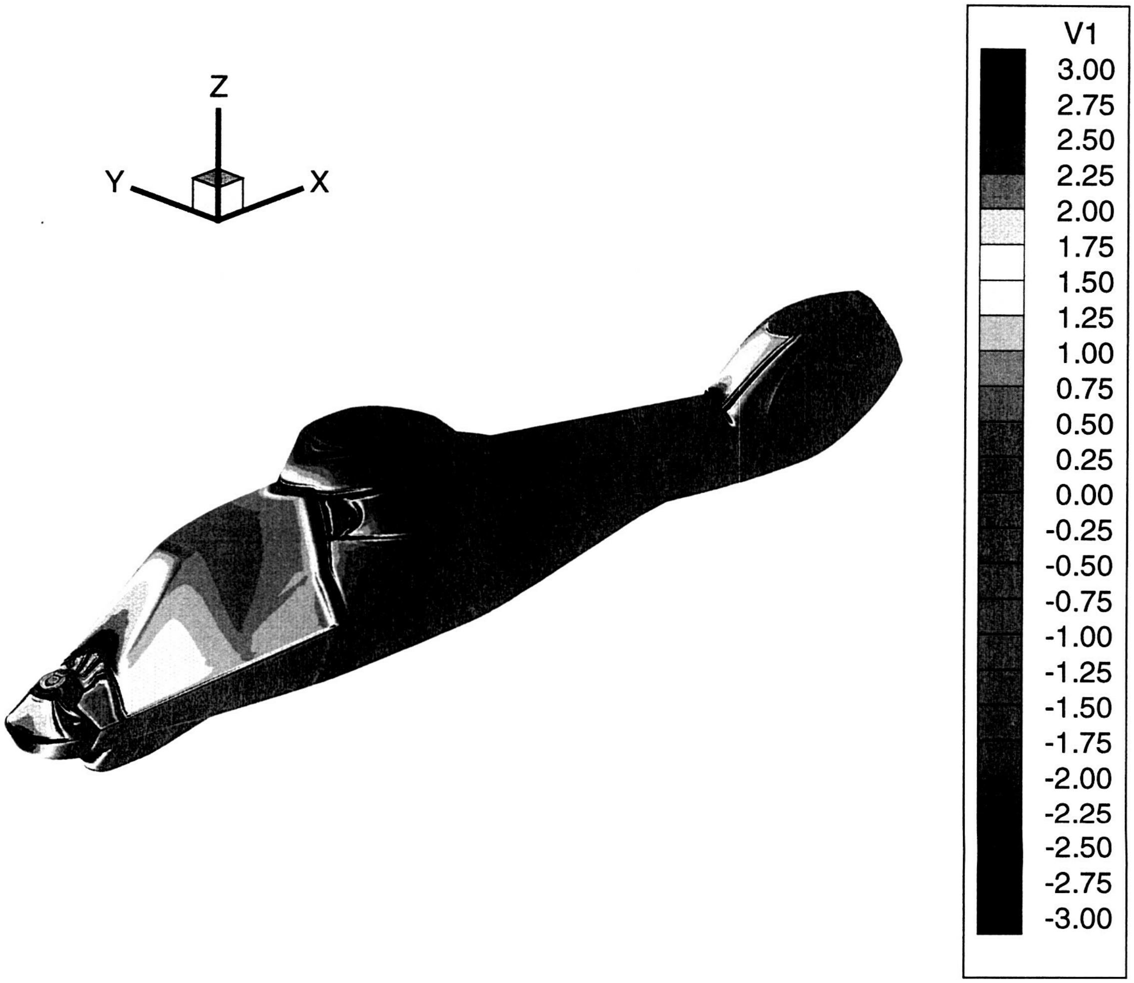

Figure 15: Comanche model fuselage surface pressure predictions

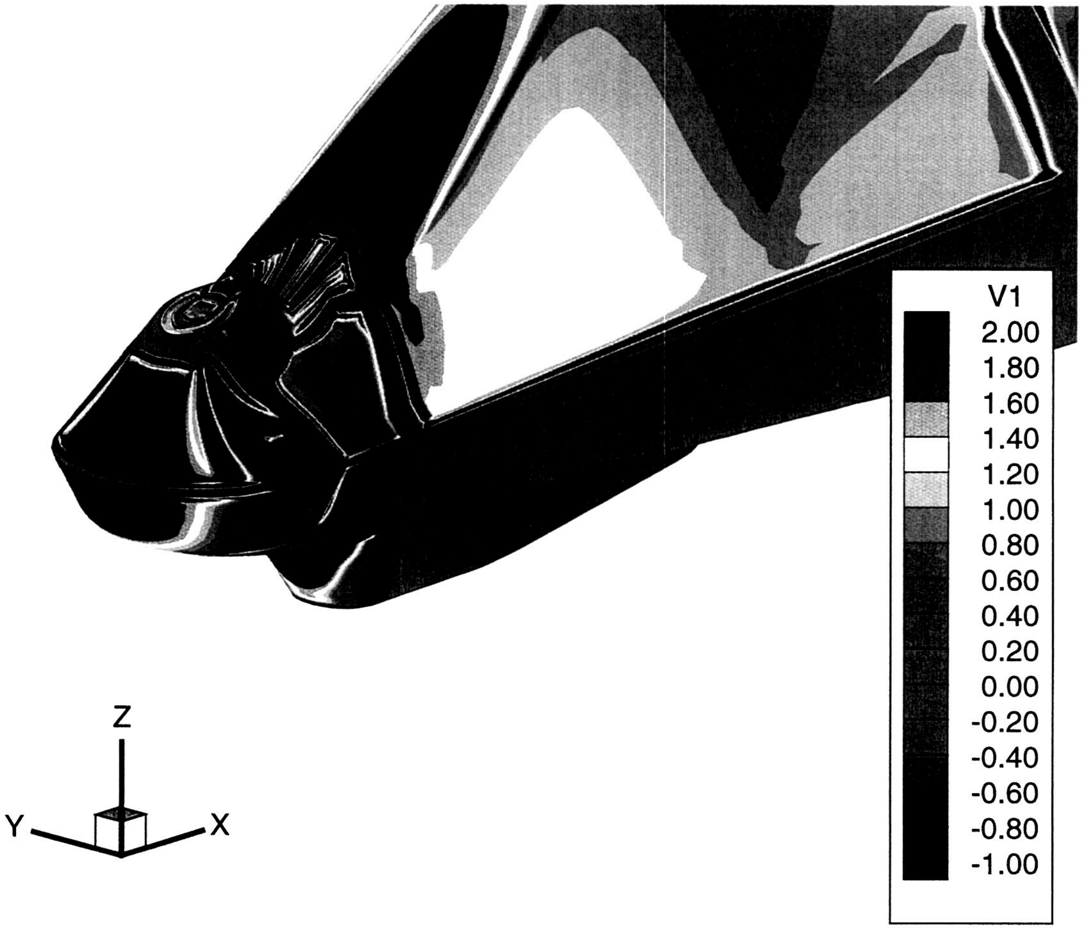

Figure 16: Comanche model fuselage surface pressure predictions on nose region

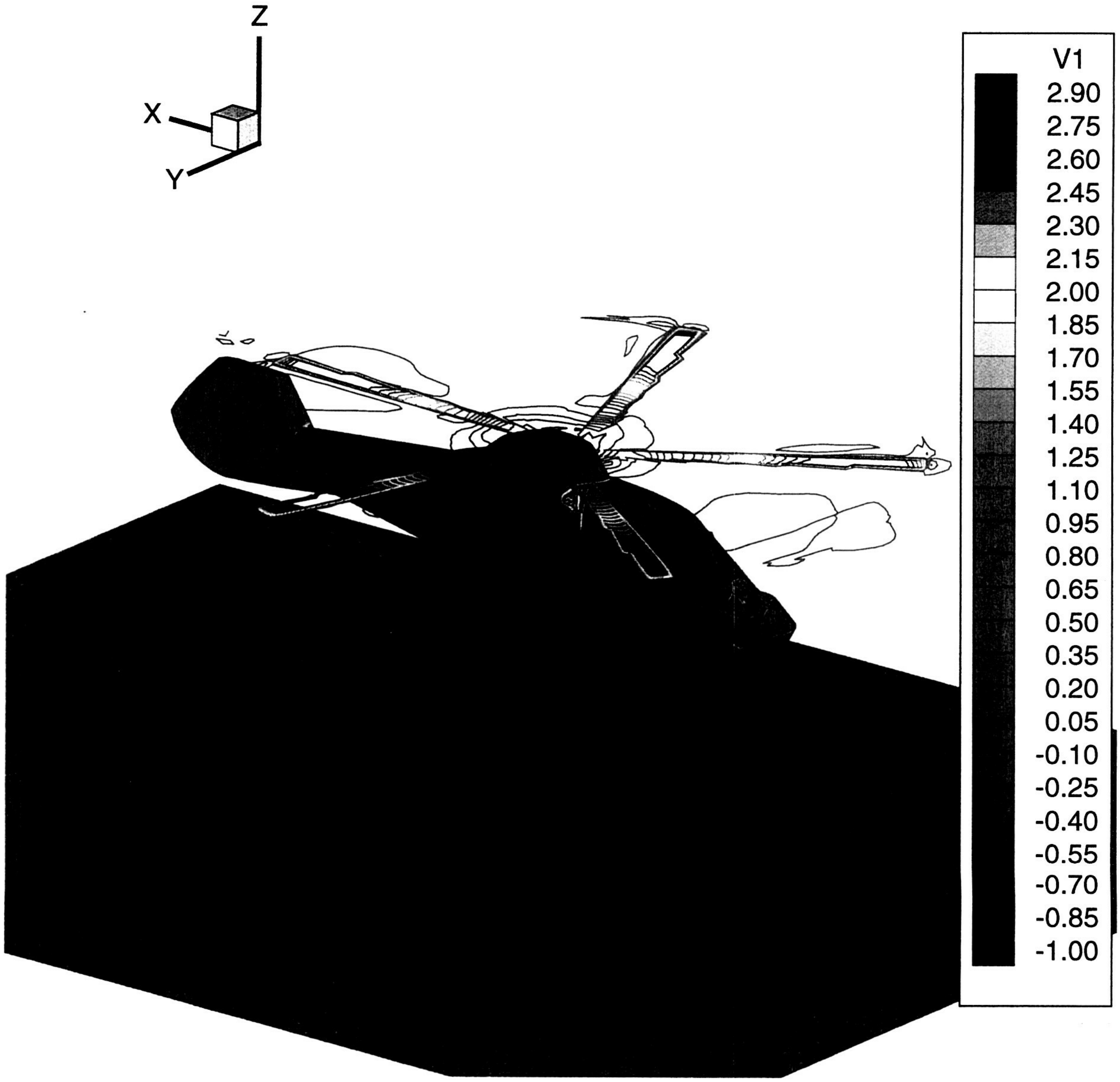

Figure 17: Comanche model pressure coefficient predictions on the fuselage and a grid plane below the main rotor